Semiconductor Physics, Quantum Electronics & Optoelectronics, 2016. V. 19, N 4. P. 404-414.
doi: https://doi.org/10.15407/spqeo19.04.404

PACS 87.50.W-

Azimuthally invariant Mueller-matrix methods in the diagnosis of liver disease

A.G. Ushenko, A.V. Dubolazov, V.A. Ushenko, Yu.A. Ushenko, M.Yu. Sakhnovskiy, M.P. Gorsky
Chernivtsi National University, 2, Kotsyubinsky str., 58012 Chernivtsi, Ukraine; e-mail: a.dubolazov@chnu.edu.ua

Abstract. Offered in this paper is the model for Mueller-matrix description mechanisms responsible for optical anisotropy typical for polycrystalline layers of histological sections taken from biological tissues and for fluids – optical activity, birefringence, as well as linear and circular dichroism. Using the statistical analysis distributions quantities of linear and circular birefringence and dichroism, the objective criteria for differentiation of myocardium histological sections (determining the cause of death), films of blood plasma (liver pathology), peritoneal fluid (endometriosis of tissues of women reproductive sphere), urine (kidney disease) have been determined. From the viewpoint of probative medicine, the operational characteristics (sensitivity, specificity and accuracy) inherent to the method of Mueller-matrix reconstruction of optical anisotropy parameters have been found.

Keywords: polarimetry, Mueller matrix, polycrystalline film, laser image, biological tissues and fluids.

Manuscript received 04.07.16; revised version received 08.09.16; accepted for publication 16.11.16; published online 05.12.16.

1. Introduction

Biological tissues and fluids represent inhomogeneous media with absorption. To describe interactions of polarized light with these complex systems, the most general approaches based on Mueller-matrix formalism are required. Nowadays, in biological and medical investigations many practical techniques based on measurements and analysis of Mueller matrices corresponding to the investigated samples are used [1-9]. In recent 10-15 years, a separate approach – laser polarimetry [10, 11] – was formed in matrix optics. On its basis, interactions between the set of statistical moments of the 1st to 4th orders characterizing Mueller-matrix elements distribution and parameters of linear birefringence of fibrillar protein networks observed in human biological tissues were determined. This enabled to diagnose oncological changes of skin derma, epithelial and connective tissue of human organs, *etc*. [12-16]. In addition, laser polarimetry techniques require further development and generalization.

First, not all elements of the Mueller matrix prove to be convenient for characterizing biological samples. The reason of this is the azimuthally dependence of the majority of matrix elements – generally 12 of 16 elements change at rotation of the sample around the probing axis.

Second, the spectrum of mechanisms of optical anisotropy in biological layers is not confined to linear birefringence only. Taking into consideration the impact

of other mechanisms – circular birefringence, and the optically anisotropic absorption (linear and circular dichroism) is topical in the aspect of enlarging the range of diagnostic techniques.

Third, there is a wide range of optically anisotropic biological objects, for which laser polarimetry techniques did not spread widely. The biological fluids – blood and its plasma, urine, bile, saliva and others – belong to them. The objects of this class are easily accessible and do not require the traumatic surgery or biopsy.

This research is focused on generalization of optical anisotropy of optically thin layers or films of biological fluids and histological sections of myocardium tissue and the development of the method of "azimuthally stable" Mueller-matrix mapping the anisotropy parameters inherent to their polycrystalline networks during differentiation of pathological and necrotic changes.

It summarizes the results of a comprehensive study of diagnostic possibilities of the method of "azimuthally stable" Mueller-matrix mapping in the following fields of medicine:

- diagnostics of myocardium necrotic changes. At present time, postmortem diagnostics of acute coronary syndrome is a leading approach in morphological [17, 18] and forensic medicine [19, 20] investigations. Balanced accuracy [21-23] of acute coronary insufficiency detection by conventional histochemical methods does not exceed 65…70% and takes relatively long time. Therefore, topical is the development of new, more accurate and express methods using the novel optical-physical approaches to formation and processing of microscopic images obtained from myocardium histological sections.
- differentiation of nonalcoholic fatty liver disease and chronic hepatitis of human liver. Liver biopsy is a "gold standard" of differential diagnostics of chronic diffuse liver disease [24, 25]. However, this method has a number of limitations and drawbacks – diagnostic errors during sampling, subjective perception of histological changes, *etc*. The conventional method of biopsy is painful for patient and exposes the risk of complication - internal bleeding, possibility of secondary infection, *etc*. [26, 27]. Therefore, an important task of modern hepatology is search for new non-invasive methods of objectification of pathological process in liver. At the same time, the objective remains the creation of an open, low-cost screening and express method of diagnostics of the severity of liver disease with an accuracy close to the gold standard.
- early detection of albuminuria is considered in this research. It is an urgent task of diagnosis of various pathological conditions of human kidney. Currently, the traditional differential diagnosis of these conditions includes the following steps: analysis of the patient's complaints, the biochemical analysis of urine protein, renal ultrasound diagnostics, professional judgment. The final step or gold standard is the nephrobiopsy of kidney tissue [28-33]. This set of techniques confidently diagnoses disease, which corresponds to a moderate (3-30 μg/μmol) and pronounced increase (>30 μg/μmol) of the protein content in the patient urine [34-36]. Along with it, the unsolved task is creation of an objective, low-cost and express screening method of albuminuria diagnostics at early stages (<30 μg/μmol) of kidney pathology close to the gold standard.
- determination of death coming prescription (DCP). At present time forensic medicine needs of essential renewal of the techniques of DCP estimation. It is related with the fact that the existing methods depend on multiple factors of external environment and circumstances of death [37-42]. The existing lack of modern, objective techniques of DCP estimation stimulates the search and development of novel techniques providing investigation of postmortem changes of human biological tissues and fluids [23, 43, 44]. Non-invasive optical methods of diagnostics of the structure of biological layers are perspective in this field.

2. Brief theoretical background

The background of our work is based on modeling representations of phase (circular and linear birefringence) and amplitude (circular and linear dichroism) anisotropy of the polycrystalline structure inherent to the biological layers.

Circular birefringence

Mueller matrix circular birefringence or optical activity of biochemical molecules has the form [8]

$$\{\Omega\} = \begin{Vmatrix} 1 & 0 & 0 & 0 \\ 0 & \omega_{22} & \omega_{23} & 0 \\ 0 & \omega_{32} & \omega_{33} & 0 \\ 0 & 0 & 0 & 1 \end{Vmatrix},$$

$$\omega_{ik} = \begin{cases} \omega_{22} = \omega_{33} = \cos 2\theta; \\ \omega_{23} = -\omega_{32} = \sin 2\theta. \end{cases} \quad (1)$$

where θ is the rotation angle of the light beam polarization plane.

$$\{F\} = \{\Omega\}\{D\} = f_{11}^{-1} \times \begin{Vmatrix} 1 & 0 & 0 & 0 \\ 0 & f_{22} & f_{23} & f_{24} \\ 0 & f_{32} & f_{33} & f_{34} \\ 0 & f_{42} & f_{43} & f_{44} \end{Vmatrix}. \quad (2)$$

The linear birefringence

Linear birefringence of molecular chains is characterized by Mueller matrix $\{D\}$ of the following form [10]

$$\{D\}=\begin{Vmatrix}1 & 0 & 0 & 0\\ 0 & d_{22} & d_{23} & d_{24}\\ 0 & d_{32} & d_{33} & d_{34}\\ 0 & d_{42} & d_{43} & d_{44}\end{Vmatrix},$$

$$d_{ik}=\begin{cases}d_{22}=\cos^2 2\rho+\sin^2 2\rho\cos\delta;\\ d_{23}=d_{32}=\cos 2\rho\sin 2\rho(1-\cos\delta);\\ d_{33}=\sin^2 2\rho+\cos^2 2\rho\cos\delta;\\ d_{42}=-d_{24}=\sin 2\rho\sin\delta;\\ d_{34}=-d_{43}=\cos 2\rho\sin\delta;\\ d_{44}=\cos\delta.\end{cases} \quad (3)$$

Here, ρ is the direction of optical axes; $\delta=\frac{2\pi}{\lambda}\Delta n l$ – phase shift between linearly polarized orthogonal components of light beam amplitude; λ – wavelength; Δn – birefringence; l – geometrical thickness.

The resulting Muller matrix of phase anisotropy takes the following form

$$\{F\}=\{\Omega\}\{D\}=f_{11}^{-1}\times\begin{Vmatrix}1 & 0 & 0 & 0\\ 0 & f_{22} & f_{23} & f_{24}\\ 0 & f_{32} & f_{33} & f_{34}\\ 0 & f_{42} & f_{43} & f_{44}\end{Vmatrix}. \quad (4)$$

Circular dichroism

Mueller matrix of circular dichroism is recorded as follows [8]

$$\{\Phi\}=\begin{Vmatrix}1 & 0 & 0 & \phi_{14}\\ 0 & \phi_{22} & 0 & 0\\ 0 & 0 & \phi_{33} & 0\\ \phi_{41} & 0 & 0 & 1\end{Vmatrix},$$

$$\phi_{ik}=\begin{cases}\phi_{22}=\phi_{33}=\dfrac{1-C^2}{1+C^2};\\ \phi_{14}=\phi_{41}=\pm\dfrac{2C}{1+C^2}.\end{cases} \quad (5)$$

Here, $C=\frac{g_\otimes-g_\oplus}{g_\otimes+g_\oplus}$, $g_\otimes$, $g_\oplus$ are absorption coefficients of left- (⊗) and right-hand (⊕) circularly polarized components of light beam amplitude.

Linear dichroism

The Mueller matrix linear dichroism is recorded as follows [8]

$$\{\Psi\}=\begin{Vmatrix}1 & \varphi_{12} & \varphi_{13} & 0\\ \varphi_{21} & \varphi_{22} & \varphi_{23} & 0\\ \varphi_{31} & \varphi_{32} & \varphi_{33} & 0\\ 0 & 0 & 0 & \varphi_{44}\end{Vmatrix},$$

$$\varphi_{ik}=\begin{cases}\varphi_{12}=\varphi_{21}=(1-\Delta\tau)\cos 2\rho;\\ \varphi_{13}=\varphi_{31}=(1-\Delta\tau)\sin 2\rho;\\ \varphi_{22}=(1+\Delta\tau)\cos^2 2\rho+2\sqrt{\Delta\tau}\sin^2 2\rho;\\ \varphi_{23}=\varphi_{32}=(1-\Delta\tau)\sin 2\rho;\\ \varphi_{33}=(1+\Delta\tau)\sin^2 2\rho+2\sqrt{\Delta\tau}\cos^2 2\rho;\\ \varphi_{44}=2\sqrt{\Delta\tau}.\end{cases} \quad (6)$$

Here, $\Delta\tau=\frac{\tau_x}{\tau_y}$, $\begin{cases}\tau_x=\tau\cos\rho;\\ \tau_y=\tau\sin\rho\end{cases}$, τ_x, τ_y are absorption coefficients of linearly polarized orthogonal components of light beam amplitude.

The resulting Mueller matrix of the generalized optical anisotropy is written in the following form

$$\{F\}=\{\Phi\}\{\Psi\}\{D\}\{\Omega\}. \quad (7)$$

Where

$$\{F\}=\prod_{i=1}^{4}\{F_i\}=f_{11}^{-1}\times\begin{Vmatrix}1 & f_{12} & f_{13} & f_{14}\\ f_{21} & f_{22} & f_{23} & f_{24}\\ f_{31} & f_{32} & f_{33} & f_{34}\\ f_{41} & f_{42} & f_{43} & f_{44}\end{Vmatrix}. \quad (8)$$

Here, $\{F_i\}$ is the Mueller matrix that characterize the phase anisotropy($\{\Omega\},\{D\}$) and also amplitude anisotropy ($\{\Phi\},\{\Psi\}$) of molecules and their aggregates.

For analytical and practical application (7), we used the data of investigations [9]. Here, it has been shown that the following elements of matrix $\{F\}$ as well as their combinations are azimuthally stable, independent of the sample rotation angle (Θ)

$$\begin{cases}f_{11}(\Theta)=\text{const};\ f_{14}(\Theta)=\text{const};\\ f_{41}(\Theta)=\text{const};\ f_{44}(\Theta)=\text{const};\end{cases}$$
$$\begin{cases}[f_{22}+f_{33}](\Theta)=\text{const};\\ [f_{23}-f_{32}](\Theta)=\text{const}.\end{cases} \quad (9)$$

3. The technique of experiment

The measurements of coordinate distributions of Mueller-matrix elements (distribution of values in the film plane of bile) were performed in the setup (Fig. 1) of the conventional Stokes-polarimeter [10].

Illumination of a sample under study was performed by the parallel ($\varnothing=10^4$) 2 laser *1* beam of "blue" semiconductor laser LSR405ML-LSR-PS-II with the wavelength λ = 0.405 μm and power W = 5 μW was used. The polarization light source consisted of quarter-

Semiconductor Physics, Quantum Electronics & Optoelectronics, 2016. V. 19, N 4. P. 404-414.
doi: https://doi.org/10.15407/spqeo19.04.404

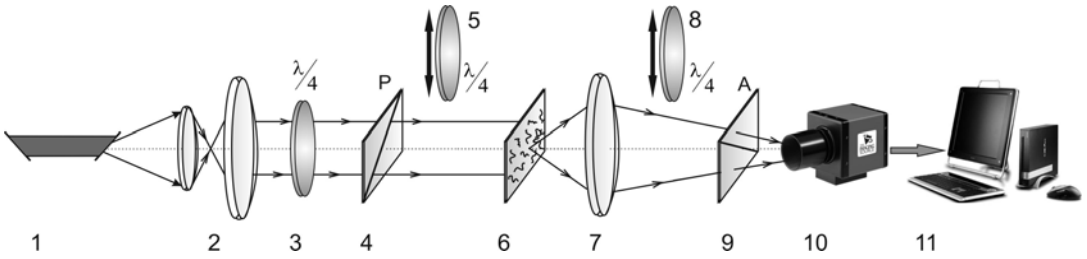

Fig. 1. Optical scheme of polarimeter: *1* – "blue" semiconductor laser; *2* – collimator; *3* – stationary quarter-wave plate; *5*, *8* – mechanically movable quarter-wave plates; *4*, *9* – polarizer and analyzer, respectively; *6* – object of investigation; *7* – polarization microobjective; *10* – CCD camera; *11* – personal computer. Explanations are in the text.

wave plates *3*, *5* and polarizer *4*, it formed a right circularly polarized beam. Polarization microobjective *7* (focal distance – 30 mm, aperture – 0.1, magnification – 4×) projected the image of biological layer *6* onto the plane of light sensitive area of CCD-camera *10*. The coordinate distribution of intensity of these fields, polarizationally filtered by the quarter-wave plate *8* and polarizer *9*, was registered by CCD-camera *10* (The Imaging Source DMK 41AU02.AS, monochrome 1/2" CCD, Sony ICX205AL (progressive scan); resolution – 1280×960; light sensitive area size – 7600×6200 μm; sensitivity – 0.05 lx; dynamic range – 8 bit; SNR – 9 bit, deviation of photosensitive characteristics from linear no more than 15%). It provided the range of measuring the structural elements of polycrystalline network with the resolution of 2…2000 μm.

For the series of linearly (0°; 45°; 90°) and right- (⊗) circularly polarized probing laser beams the Stokes-vector parameters $S_{i=2;3;4}^{0;45;90;\otimes}$ were measured in the points of the digital image

$$\begin{cases} S_{i=2}^{0;45;90;\otimes} = I_0{}^{0;45;90;\otimes} + I_{90}{}^{0;45;90;\otimes}; \\ S_{i=2}^{0;45;90;\otimes} = I_0{}^{0;45;90;\otimes} - I_{90}{}^{0;45;90;\otimes}; \\ S_{i=3}^{0;45;90;\otimes} = I_{45}^{0;45;90;\otimes} - I_{135}^{0;45;90;\otimes}; \\ S_{i=4}^{0;45;90;\otimes} = I_{\otimes}{}^{0;45;90;\otimes} - I_{\oplus}{}^{0;45;90;\otimes}. \end{cases} \quad (10)$$

Here, $I_{0;90;45;135;\otimes;\oplus}^{0;45;90;\otimes}$ are the intensities of linearly (0°; 90°; 45°; 135°), right- (⊗) and left- (⊕) circularly polarized components of the filtered (by means of polarizer *9* and quarter-wave plate *8*) laser radiation.

Further the Mueller-matrix invariants were calculated

$$\begin{cases} f_{14} = S_1^{\otimes} - 0.5\left(S_1^0 + S_1^{90}\right); \\ f_{41} = 0.5\left(S_4^0 + S_4^{90}\right); \\ f_{44} = S_4^{\otimes} - 0.5\left(S_4^0 + S_4^{90}\right); \\ \Delta f = \dfrac{f_{23} - f_{32}}{f_{22} + f_{33}} = \dfrac{S_2^{45} - 0.5\left(S_2^0 + S_2^{90}\right) - 0.5\left(S_3^0 - S_3^{90}\right)}{0.5\left(S_2^0 - S_2^{90}\right) + S_3^{45} - 0.5\left(S_3^0 + S_3^{90}\right)}. \end{cases} \quad (11)$$

For objective assessment of coordinate distributions $q \equiv \begin{cases} f_{14;41;44}(m \times n) \\ \Delta f(m \times n) \end{cases}$, we applied the synthesis of traditional methods of statistical and correlation analysis.

A set of statistical moments of the 1st to 4th orders characterizing distributions q was calculated using the algorithms

$$Z_1 = \frac{1}{N}\sum_{j=1}^{N}|q|_j;\ Z_2 = \sqrt{\frac{1}{N}\sum_{j=1}^{N}(q - Z_1)_j{}^2};$$

$$Z_3 = \frac{1}{Z_2{}^3}\frac{1}{N}\sum_{j=1}^{N}(q - Z_1)_j^3;\ Z_4 = \frac{1}{Z_2{}^4}\frac{1}{N}\sum_{j=1}^{N}(q - Z_1)_j{}^4. \quad (12)$$

N – the number of pixels of CCD-camera.

4. Algorithm of statistical analysis of Muller-matrix imaging

The following part of the research consists in investigation of the efficiency in application of the method based on azimuthally stable Mueller-matrix mapping the polycrystalline structures of biological layers in differential diagnosis of both pathological and necrotic states inherent to human tissues and fluids.

It comprises a number of tasks topical for medicine applications, solving of which by means of conventional histological methods is complicated or require considerable time.

The technique of differential diagnosis of optical anisotropy parameters (1-5) for polycrystalline networks of biological layers includes the following stages:

1. Formation of the representative sampling of samples for both reference and research groups – group 1 and group 2, correspondingly. The differentiation between group 1 and group 2 was determined using the gold standard method. By means of software product Seatmate for 95% confidence interval ($p < 0.05$), the reliable quantity of people (samples) was determined – $n = N_0$.
2. Measurement of the coordinate distributions for values of Mueller-matrix invariants $q = \{M_{14;\,41;\,44};\, \Delta M\}$.

3. Calculation of the set of statistic moments of the 1st to 4th orders for each distribution $q(m \times n)$.
4. The size of a representative sampling was tested using cross-validation. It was ascertained that the average value of the standard deviation for the statistical moments $Z_{i=1;2;3;4}$ do not exceed 0.025, which corresponds to a statistically valid confidence interval $p < 0.05$.
5. For the possible clinical application of both methods, the following characteristics were determined for each group of the samples [44-46]:
   - average (within group 1 and group 2) values of statistical moments $\overline{Z}_{i=1;2;3;4}(q)$, their standard deviations $\pm\sigma$ and histograms $N(Z_i)$;
   - traditional for probative medicine operational characteristics – sensitivity $\left(Se = \frac{a}{a+b}100\%\right)$, specificity $\left(Sp = \frac{c}{c+d}100\%\right)$ and balanced accuracy $\left(Ac = \frac{Se+Sp}{2}\right)$, where a and b are the numbers of correct and wrong diagnoses within the group 2; c and d – the same within group 1.

5. Differentiation of necrotic changes in myocardium polycrystalline networks

As the objects of investigation, we used the optically thin histological sections of myocardium tissue of dead people, the death was caused by the ischemic heart disease (group 1 – 38 samples) and by acute coronary insufficiency (group 2 – 38 samples). The histological sections were prepared using the conventional procedure by means of freezing microtome. The geometrical thickness of samples was $d = 25…30$ μm, attenuation coefficient was $\tau = 0.086…0.093$.

The series of Figs. 2 and 3 presents topology and histograms of values of Mueller-matrix invariants $q(m \times n)$ corresponding to the histological sections of myocardium tissue for the groups 1 and 2, which show to the influence of phase (Fig. 2) and amplitude (Fig. 3) anisotropies.

Table 1 presents the results of intergroup statistic analysis and balanced accuracy of the method of azimuthally stable Mueller-matrix mapping the myocardium histological sections during the differentiation of death cases caused by the ischemic heart disease and acute coronary insufficiency.

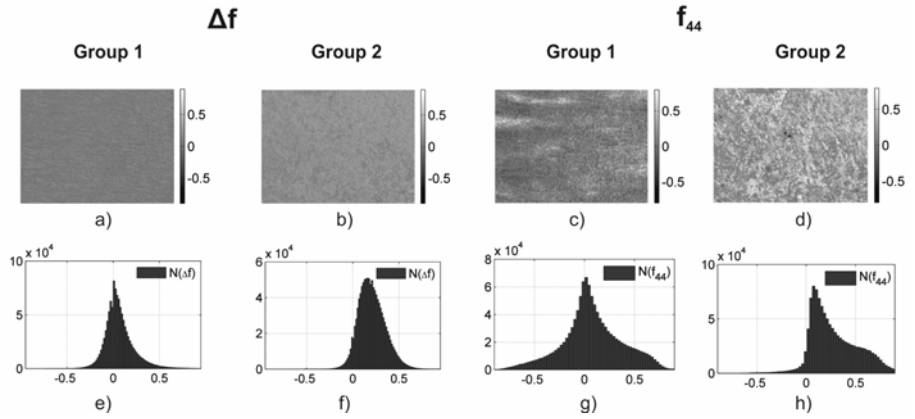

Fig. 2. Topology and histograms of values of Mueller-matrix invariants $q(m \times n)$ for phase anisotropy of myocardium histological sections for the groups 1 and 2.

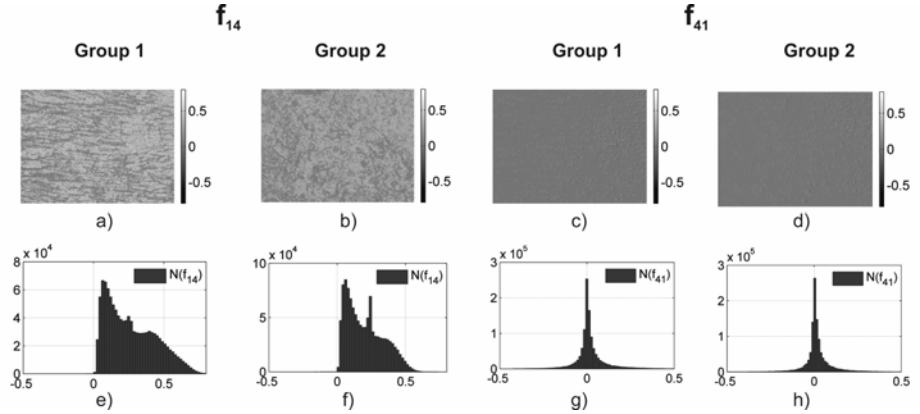

Fig. 3. Topology and histograms of values of Mueller-matrix invariants $q(m \times n)$ for amplitude anisotropy of myocardium histological sections in the groups 1 and 2.

Table 1. Average ($\overline{Z}_{i=1;2;3;4}$), standard deviation (±σ) of statistical moments $Z_{i=1;2;3;4}$ and balanced accuracy of the method.

$\overline{Z}_{i=1;2;3;4}$	Δf			f_{44}			f_{14}			f_{41}		
	Group 1	Group 2	Ac,%	Group 1	Group 2	Ac,%	Group 1	Group 2	Ac, %	Group 1	Group 2	Ac,%
$\overline{Z}_1$	0.07 ± 0.007	0.1 ± 0.008	58	0.075 ± 0.005	0.085 ± 0.006	59	0.32 ± 0.021	0.25 ± 0.014	71	0.04 ± 0.003	0.03 ± 0.002	54
$\overline{Z}_2$	0.19 ± 0.018	0.27 ± 0.021	73	0.33 ± 0.022	0.19 ± 0.012	85	0.19 ± 0.012	0.14 ± 0.01	65	0.08 ± 0.005	0.11 ± 0.07	68
$\overline{Z}_3$	0.12 ± 0.09	0.15 ± 0.094	57	0.35 ± 0.024	0.67 ± 0.047	96	1.78 ± 0.12	0.91 ± 0.08	92	0.17 ± 0.012	0.22 ± 0.016	73
$\overline{Z}_4$	0.14 ± 0.013	0.23 ± 0.016	69	0.67 ± 0.051	0.91 ± 0.075	82	0.86 ± 0.067	1.12 ± 0.093	84	1.25 ± 0.09	1.38 ± 0.11	64

Table 2. Average ($\overline{Z}_{i=1;2;3;4}$), standard deviation (±σ) of statistical moments $Z_{i=1;2;3;4}$ and balanced accuracy of the method.

$\overline{Z}_{i=1;2;3;4}$	Δf			f_{44}			f_{14}			f_{41}		
	Group 1	Group 2	*Ac*,%	Group 1	Group 2	*Ac*,%	Group 1	Group 2	Ac,%	Group 1	Group 2	*Ac*,%
$\overline{Z}_1$	0.07 ± 0.005	0.05 ± 0.003	67	0.11 ± 0.07	0.18 ± 0.012	82	0.11 ± 0,07	0.08 ± 0.006	75	0.09 ± 0.07	0.07 ± 0.006	65
$\overline{Z}_2$	0.16 ± 0.011	0.09 ± 0.006	84	0.29 ± 0.017	0.24 ± 0.015		0.14 ± 0.09	0.105 ± 0 .07	72	0.11 ± 0.07	0.13 ± 0.09	71
$\overline{Z}_3$	0.39 ± 0.021	0.62 ± 0.037	91	1.85 ± 0.13	0.91 ± 0.077	92	1.61 ± 0.11	1.89 ± 0.14	67	1.36 ± 0.11	1.49 ± 0.14	59
$\overline{Z}_4$	0.41 ± 0.028	0.79 ± 0.058	90	1.24 ± 0.098	0.79 ± 0.058	90	2.11 ± 0.17	2.35 ± 0.19	69	1.31 ± 0.11	1.85 ± 0.13	82

The maximum accuracy of differentiation of death cases caused by the ischemic heart disease and acute coronary insufficiency by means of statistic analysis of $\overline{Z}_3(f_{44}, f_{14})$ is 92…96% (marked out by gray color) corresponds to excellent quality of diagnostic test [44].

6. Diagnostics and differentiation of the degree of liver pathology

As the objects of investigation, we used the optically thin polycrystalline films of blood plasma taken from patients with the non-alcoholic fatty liver disease (group 1 – 48 samples) and chronic hepatitis (group 2 – 48 samples). The films of blood plasma were prepared by means of putting a drop of plasma on an optically isotropic glass with following drying at room temperature. The geometrical thickness of films was d = 10…15 μm, attenuation coefficient was τ = 0.068…0.073.

The series of Figs. 4 and 5 presents topology and histograms of values of Mueller-matrix invariants $q(m \times n)$ for the polycrystalline films of blood plasma taken from patients of the groups 1 and 2, which correspond to the influence of phase (Fig. 4) and amplitude (Fig. 5) anisotropies.

Table 2 presents the results of intergroup statistic analysis and balanced accuracy of the method providing azimuthally stable Mueller-matrix mapping the films of blood plasma during differentiation between the non-alcoholic fatty liver disease and chronic hepatitis.

The maximum accuracy of differentiation of liver pathology by means of statistic analysis of $\overline{Z}_3(\Delta f, f_{44})$ and $\overline{Z}_4(\Delta f, f_{44})$ is 90…92% (marked out by gray color) corresponds to good quality of diagnostic test [44].

7. Diagnostics of human kidney albuminuria

As the objects of investigation, we used the optically thin polycrystalline films of urine of donors (group 1 – 57 samples) and patients with albuminuria (early stage < 3μg/μmol) (group 2 – 57 samples). The films of urine fluid were prepared similarly to the films of blood plasma.

The series of Figs. 6 and 7 presents topology and histograms for values of Mueller-matrix invariants $q(m \times n)$ corresponding to the polycrystalline films of urine fluid taken from patients of the groups 1 and 2, which demonstrate the influence of phase (Fig. 6) and amplitude (Fig. 7) anisotropies.

Table 3 presents the results of intergroup statistic analysis and balanced accuracy inherent to the method of azimuthally stable Mueller-matrix mapping the films of urine fluid during the differentiation between donors and patients with albuminuria.

The maximum accuracy of diagnosing albuminuria (< 3μg/μmol) by means of statistic analysis of $\overline{Z}_{2;3;4}(f_{44})$; $\overline{Z}_{3;4}(f_{41})$ is 91…94% (marked out by gray color) corresponds to the excellent quality of diagnostic test [44].

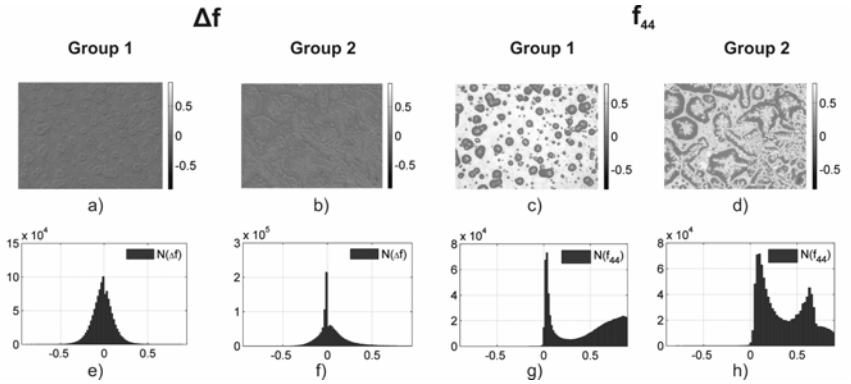

Fig. 4. Topology and histograms of values of Mueller-matrix invariants $q(m \times n)$ for phase anisotropy in polycrystalline films of blood plasma taken from patients of the groups 1 and 2.

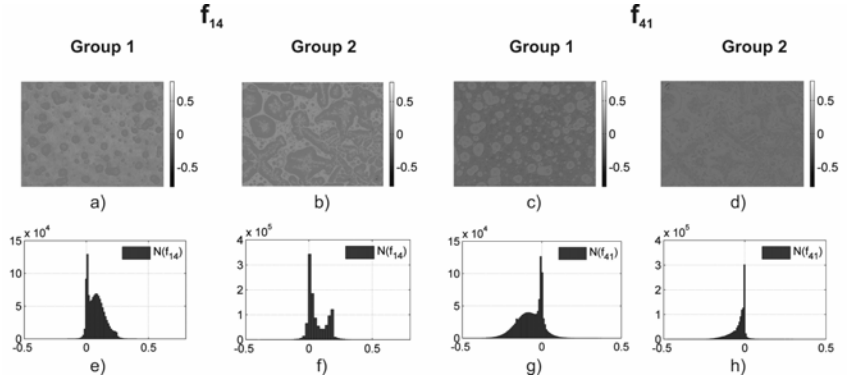

Fig. 5. Topology and histograms of values of Mueller-matrix invariants $q(m \times n)$ for amplitude anisotropy in polycrystalline films of blood plasma taken from patients of the groups 1 and 2.

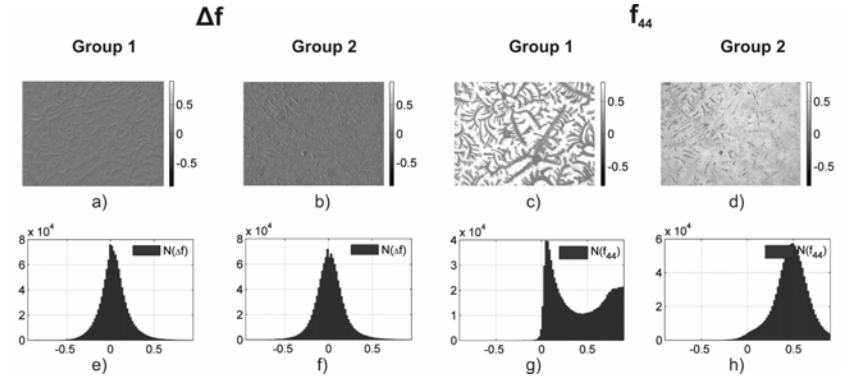

Fig. 6. Topology and histograms of values of Mueller-matrix invariants $q(m \times n)$ for phase anisotropy in polycrystalline films of urine fluid taken from patients of the groups 1 and 2.

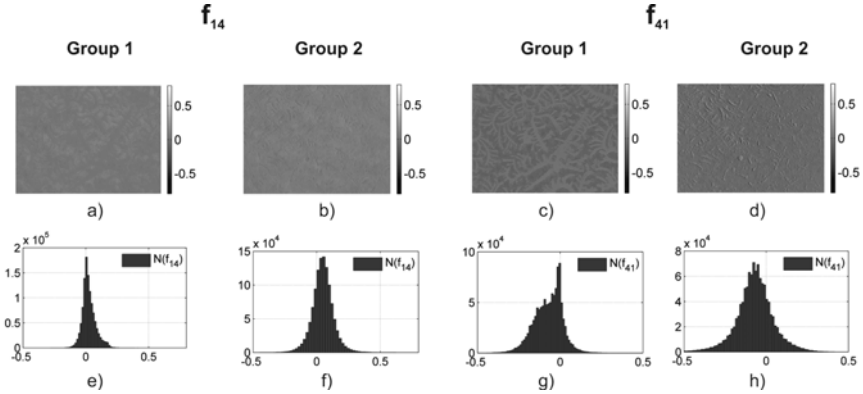

Fig. 7. Topology and histograms of values of Mueller-matrix invariants $q(m \times n)$ for amplitude anisotropy in polycrystalline films of urine fluid taken from patients of the groups 1 and 2.

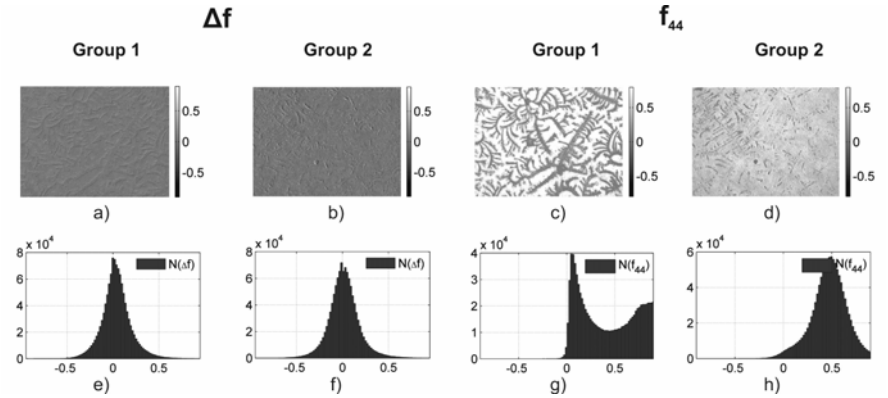

Fig. 8. Topology and histograms of values of Mueller-matrix invariants $q(m \times n)$ for phase anisotropy observed in polycrystalline films of liquor fluid of the groups 1 and 2.

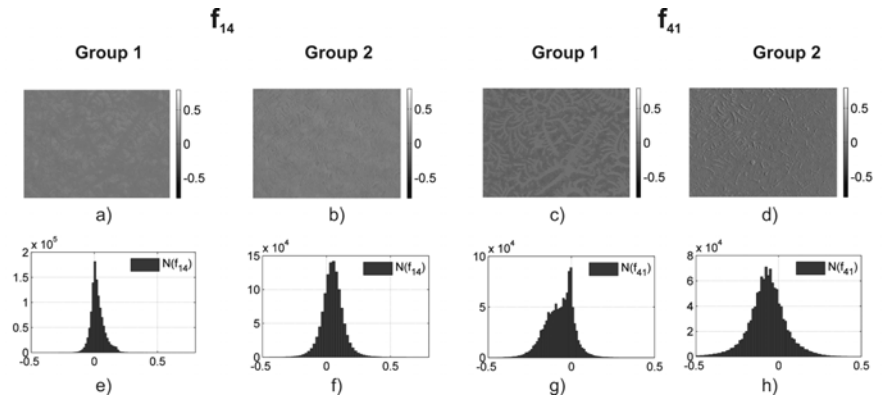

Fig. 9. Topology and histograms of values of Mueller-matrix invariants $q(m \times n)$ for amplitude anisotropy observed in polycrystalline films of liquor fluid of the groups 1 and 2.

Table 3. Average ($\overline{Z}_{i=1;2;3;4}$), standard deviation (±σ) of statistical moments $Z_{i=1;2;3;4}$ and balanced accuracy of the method.

$\overline{Z}_{i=1;2;3;4}$	Δf			f_{44}			f_{14}			f_{41}		
	Group 1	Group 2	*Ac*,%	Group 1	Group 2	*Ac*,%	Group 1	Group 2	*Ac*,%	Group 1	Group 2	*Ac*,%
$\overline{Z}_1$	0.08 ± 0.006	0.09 ± 0.007	54	0.34 ± 0.023	0.45 ± 0.037	73	0.06 ± 0.004	0.08 ± 0.007	61	0.12 ± 0.009	0.15 ± 0.01	67
$\overline{Z}_2$	0.17 ± 0.012	0.14 ± 0.09	67	0.32 ± 0.024	0.23 ± 0.016	75	0.09 ± 0.007	0.11 ± 0.009	66	0.16 ± 0.011	0.18 ± 0.013	62
$\overline{Z}_3$	0.11 ± 0.007	0.14 ± 0.009	66	1.43 ± 0.11	0.74 ± 0.057	94	0.66 ± 0.042	0.53 ± 0.038	75	1.13 ± 0.092	0.69 ± 0.041	91
$\overline{Z}_4$	0.31 ± 0.021	0.49 ± 0.028	79	1.54 ± 0.12	0.89 ± 0.065	91	0.81 ± 0.064	0.98 ± 0.077	80	1.71 ± 0.014	0.87 ± 0.069	94

Table 4. Time dependences of statistical moments of the 3rd and 4th orders, which characterize Mueller-matrix invariants distributions $q(m \times n)$ for polycrystalline liquor films of human corpse.

T, hours	1	6	12	24	36	48
Δf						
Z_3	0.19 ± 0.009	0.58 ± 0.042	1.04 ± 0.086	1.03 ± 0.091	1.07 ± 0.093	1.02 ± 0.082
Z_4	0.53 ± 0.041	1.11 ± 0.099	1.67 ± 0.12	1.63 ± 0.12	1.69 ± 0.12	1.63 ± 0.12
f_{44}						
Z_3	1.03 ± 0.088	1.28 ± 0.097	1.55 ± 0.11	1.82 ± 0,14	2.07 ± 0.16	2.34 ± 0.18
Z_4	1.15 ± 0.093	1.54 ± 0.11	1.97 ± 0.14	2.32 ± 0.19	2.71 ± 0.21	3.26 ± 0.26
f_{14}						
Z_3	0.52 ± 0.034	0.71 ± 0.054	0.82 ± 0.067	0.81 ± 0.065	0.84 ± 0.07	0.81 ± 0.066
Z_4	0.63 ± 0.041	0.89 ± 0.071	1.11 ± 0.093	1.09 ± 0.091	1.08 ± 0.089	1.11 ± 0.096
f_{41}						
Z_3	1.21 ± 0.095	1.39 ± 0.098	1.58 ± 0.12	1.77 ± 0.14	1.99 ± 0.16	2.17 ± 0.18
Z_4	1.37 ± 0.11	1.51 ± 0.11	1.69 ± 0.013	1.94 ± 0.16	2.21 ± 0.18	2.38 ± 0.19

8. Diagnostics of death coming prescription

The following group were used as objects of investigation in this research: postmortal polycrystalline liquor films received from the patients who died of myocardial infarction (48 samples).

Experimental study of time dynamics of postmortal change in the biochemical structure of liquor films was performed using the following algorithm:

1. For each sample of polycrystalline liquor films, the coordinate distributions of Mueller-matrix invariants $q(m \times n)$ values were determined.
2. The measurement of $q(m \times n)$ in the polycrystalline liquor films was performed in two stages: 1st – every 15 min during 6 hours from the moment of death; 2nd – every hour up to 48 hours after the moment of death.
3. For each distribution of Mueller matrix values, the statistical moments of the 1st-4th order were calculated.
4. The time dependences of the change in the statistical moments are most sensitive to necrotic changes until the stabilization value of these parameters is achieved.

The series of Figs. 8 and 9 presents topology and histograms of values of Mueller-matrix invariants $q(m \times n)$ for the polycrystalline films of liquor after 1 hour (group 1) and 12 hours (group 2) after death coming, which correspond to the necrotic changes in phase (Fig. 8) and amplitude (Fig. 9) anisotropies.

Time monitoring of post-mortal changes in Mueller-matrix invariants maps of liquor films proves the most dynamic change in the statistical moments of the 3rd and 4th orders (Table 4).

It follows from the time monitoring of changes in the statistical structure of Mueller-matrix elements distributions typical for polycrystalline networks of liquor films that the interval of DCP determination is T = 12…48 hours.

The following intervals and accuracy of DCP determination are presented in Table 5.

Table 5. Intervals and accuracy of DCP determination.

Parameters	Interval of DCP determination, T	Accuracy of DCP determination, ΔT
Distribution of Δf	12 hours	25 min
Distribution of f_{44}	48 hours	45 min
Distribution of f_{14}	14 hours	25 min
Distribution of f_{41}	48 hours	45 min

9. Conclusions

1. The Mueller-matrix model of generalized phase and amplitude anisotropy in polycrystalline networks of biological tissues and fluids taken from human organs has been developed.
2. It has been proposed the new method for mapping both the histological sections of biological tissues and polycrystalline films of biological fluids by means of measuring the coordinate distributions of values in the set of Mueller-matrix invariants.
3. Practical approbation of azimuthally stable Mueller-matrix mapping the biological layers in a number of applications in medical diagnostics by means of statistic analysis of coordinate distributions of values of the matrix elements $f_{44;41;14}$ and $\Delta f = \dfrac{f_{23} - f_{32}}{f_{22} + f_{33}}$ has been performed. The balanced accuracy of diagnostic test has been determined.
4. It has been found that:
   - balanced accuracy in differentiation of death cases caused by the ischemic heart disease and acute coronary insufficiency is 92…96% – corresponds to the excellent quality of diagnostic test for Mueller-matrix mapping the myocardium histological sections;
   - balanced accuracy in differentiation of the stage of liver pathology is 90…92% – corresponds to the good quality of diagnostic test for Mueller-matrix mapping the polycrystalline films of blood plasma;
   - balanced accuracy in diagnostics of endometriosis is 89…91% – corresponds to the good quality of diagnostic test for Mueller-matrix mapping the polycrystalline films of peritoneal fluid;
   - balanced accuracy in diagnostics of albuminuria is 91…94% – corresponds to the excellent quality of diagnostic test for Mueller-matrix mapping the polycrystalline films of urine fluid.

References

1. T.T. Tower, R.T. Tranquillo, Alignment maps of tissues: I. Microscopic elliptical polarimetry // *Biophys. J.* **81**, p. 2954-2963 (2001).
2. J.M. Bueno, J. Jaronski, Spatially resolved polarization properties for in vitro corneas // *Ophthal., Physiol. Opt.* **21**, No. 5, p. 384-392 (2001).
3. M.H. Smith, Interpreting Mueller matrix images of tissues // *Proc. SPIE*, **4257**, p. 82-89 (2001).
4. M.H. Smith, P. Burke, A. Lompado, E. Tanner, L.W. Hillman, Mueller matrix imaging polarimetry in dermatology // *Proc. SPIE*, **3991**, p. 210-216 (2000).

5. J.M. Bueno, F. Vargas-Martin, Measurements of the corneal birefringence with a liquid-crystal imaging polariscope // *Appl. Opt*. **41**, p. 116-124 (2002).
6. T.T. Tower, R.T. Tranquillo, Alignment maps of tissues: II. Fast harmonic analysis for imaging // *Biophys. J*. **81**, p. 2964-2971 (2001).
7. M. Shribak and R. Oldenbourg, Techniques for fast and sensitive measurements of two-dimensional birefringence distributions // *Appl. Opt*. **42**, p. 3009-3017 (2003).
8. S.N. Savenkov, V.V. Marienko, E.A. Oberemok, O.I. Sydoruk, Generalized matrix equivalence theorem for polarization theory // *Phys. Rev. E*, **74**, p. 605-607 (2006).
9. S.-Y. Lu, R.A. Chipman, Interpretation of Mueller matrices based on polar decomposition // *J. Opt. Soc. Am. A*, **13**, p. 1106-1113 (1996).
10. A.G. Ushenko and V.P. Pishak, Laser Polarimetry of Biological Tissue: Principles and Applications, in: *Handbook of Coherent-Domain Optical Methods: Biomedical Diagnostics*, *Environmental and Material Science*, Vol. 1, p. 93-138, ed. by V.V. Tuchin. Kluwer Academic Publishers, 2004.
11. Yu.A. Ushenko, T.M. Boychuk, V.T. Bachynsky, O.P. Mincer, Diagnostics of structure and physiological state of birefringent biological tissues: Statistical, correlation and topological approaches, in: *Handbook of Coherent-Domain Optical Methods*. Springer Science+Business Media, New York, 2013, p. 107-148.
12. A.G. Ushenko, D.N. Burkovets, Yu.A. Ushenko, Polarization phase mapping and reconstruction of biological tissue architectonics during diagnosis of pathological lesion // *Optics and Spectroscopy*, **93**(3), 449-456 (2002).
13. V.A. Ushenko, M.P. Gorsky, Complex degree of mutual anisotropy of linear birefringence and optical activity of biological tissues in diagnostics of prostate cancer // *Optics and Spectroscopy*, **115**(2), 290-297 (2013).
14. Yu.A. Ushenko, M.P. Gorskii, A.V. Dubolazov, A.V. Motrich, V.A. Ushenko, M.I. Sidor, Spatial-frequency Fourier polarimetry of the complex degree of mutual anisotropy of linear and circular birefringence in the diagnostics of oncological changes in morphological structure of biological tissues // *Quantum Electronics*, **42**(8), p. 727 (2012).
15. A. Ushenko, S. Yermolenko, A. Prydij et al., Statistical and fractal approaches in laser polarimetry diagnostics of the cancer prostate tissues // *Proc. SPIE*, **7008**, art. no. 70082C (2008).
16. O.V. Angelsky, A.G. Ushenko, Y.G. Ushenko, Complex degree of mutual polarization of biological tissue coherent images for the diagnostics of their physiological state // *J. Biomed. Opt.* **10**(6), p. 060502-060502-3 (2005).
17. A.G. Ushenko, Laser diagnostics of biofractals // *Quantum Electronics*, **29**(12), p. 1074-1077 (1999).
18. V.A. Holovatsky, O.M. Makhanets, O.M. Voitsekhivska, Oscillator strengths of electron quantum transitions in spherical nanosystems with donor impurity in the center // *Physica E: Low-Dimension. Systems and Nanostruct*. **41**(8), p. 1522-1526 (2009).
19. M.D. Pérez-Cárceles, J. Noguera, J.L. Jiménez, P. Martínez, A. Luna, E. Osuna, Diagnostic efficacy of biochemical markers in diagnosis post-mortem of ischaemic heart disease // *Forensic Sci. Int.* **142**, p. 1-7 (2004).
20. F. Martínez Díaz, M. Rodríguez-Morlensín, M.D. Pérez-Cárceles, J. Noguera, A. Luna and E. Osuna, Biochemical analysis and immune-histochemical determination of cardiac troponin for the postmortem diagnosis of myocardial damage // *Histol. Histopathol*. **20**, p. 475-481 (2005).
21. O.V. Angelsky, C.Y. Zenkova, M.P. Gorsky, N.V. Gorodyńska, Feasibility of estimating the degree of coherence of waves at the near field // *Appl. Opt.* **48**(15), p. 2784-2788 (2009).
22. C.S. Davis, *Statistical Methods of the Analysis of Repeated Measurements*. New York, Springer-Verlag, 2002, p. 744.
23. A. Petrie, B. Sabin, *Medical Statistics at a Glance.* Blackwell Publ. 2005, p. 157.
24. O.V. Angel'skii, A.G. Ushenko, A.D. Arkhelyuk, S.B. Ermolenko, D.N. Burkovets, Structure of matrices for the transformation of laser radiation by biofractals // *Quantum Electronics*, **29**(12), p. 1074-1077 (1999).
25. O.V. Angel'skii, A.G. Ushenko, A.D. Arkhelyuk, S.B. Ermolenko, D.N. Burkovets, Scattering of laser radiation by multifractal biological structures // *Optics and Spectroscopy*, **88**(3), p. 444-447 (2000).
26. D. van Beek, B. Funaki, Hemorrhage as a complication of percutaneous liver biopsy // *Semin. Intervent. Radiol*. Dec **30**(4), p. 413-416 (2013).
27. O.V. Angelsky, R.N. Besaha, A.I. Mokhun, I.I. Mokhun, M.O. Sopin, M.S. Soskin, M.V. Vasnetsov // Singularities in vectoral fields // *Proc. SPIE*, **3904**, p. 40 (1999).
28. N. Boute, O. Gribouval, S. Roselli et al., NPHS2, encoding the glomerular protein podocin, is mutated in autosomal recessive steroid-resistant nephrotic syndrome // *Nat. Genet*. **24**(4), p. 349-354 (2000).
29. B.M. Brenner, *The Kidney*. Brenner and Rector's 8-th Ed. 2007.
30. Y.T. Chen, A. Kobayashi, K.M. Kwan et al., Gene expression profiles in developing nephrons using *Lim1* metanephric mesenchyme-specific conditional mutant mice // *BMC Nephrol.* **7**, issue 1, Article 1 (2006).
31. P.N. Hawkins, Serum amyloid P component scintigraphy for diagnosis and monitoring amyloidosis // *Curr. Opin. Nephrol. Hypertens*. **11**, p. 649-655 (2002).

32. B.G. Hudson, K. Tryggvason, M. Sundaramoorthy, E.G. Neilson, Alport's syndrome, Goodpasture's syndrome, and type IV collagen // *N. Engl. J. Med*. **348**, p. 2543-2556 (2003).
33. KDIGO 2012 Clinical Practice Guidelines for the Evaluation and Management of Chronic Kidney Disease // *Kidney Int. Suppl.* **3**, Issue 1 (2013).
34. V.A. Ushenko, M.I. Sidor, Y.F. Marchuk, N.V. Pashkovskaya, D.R. Andreichuk, Azimuth-invariant Mueller-matrix differentiation of the optical anisotropy of biological tissues // *Optics and Spectroscopy*, **117**(1), p. 152-157 (2014).
35. V.A. Ushenko, N.I. Zabolotna, S.V. Pavlov, D.M. Burcovets, O.Yu. Novakovska, Mueller-matrices polarization selection of two-dimensional linear and circular birefringence images // *Proc. SPIE*, **9066**, Eleventh International Conference on Correlation Optics, 90661X (2013).
36. V.A. Ushenko, M.P. Gorsky, Complex degree of mutual anisotropy of linear birefringence and optical activity of biological tissues in diagnostics of prostate cancer // *Optics and Spectroscopy*, **115**(2), p. 290-297 (2013).
37. Yu.A. Ushenko, M.P. Gorsky, A.V. Dubolazov, A.V. Motrich, V.A. Ushenko, M.I. Sidor, Spatial-frequency Fourier polarimetry of the complex degree of mutual anisotrospy of linear and circular birefringence in the diagnostics of oncological changes in morphological structure of biological tissues // *Quantum Electronics*, **42**(8), p. 727 (2012).
38. V.A. Ushenko, Complex degree of mutual coherence of biological liquids, in: *ROMOPTO International Conference on Micro- to Nano-Photonics III* (pp. 88820V-88820V), International Society for Optics and Photonics, 2013.
39. F. Brion, B. Marc, F. Launay, Postmortem interval estimation by creatinine levels in human psoas muscle // *Forensic Sci. Int.* **52**(1), p. 113-120 (1991).
40. L.D. Cassidy, Basic concepts of statistical analysis for surgical research // *J. Surgical Res.* **128**, p. 199-206 (2005).
41. Yu.O. Ushenko, O.V. Dubolazov, A.O. Karachevtsev, M.P. Gorsky, Y.F. Marchuk, Wavelet analysis of Fourier polarized images of the human bile // *Appl. Opt.* **51**(10), p. C133-C139 (2012).
42. Yu.A. Ushenko, V.A. Ushenko, A.V. Dubolazov, V.O. Balanetskaya, N.I. Zabolotna, Mueller-matrix diagnostics of optical properties of polycrystalline networks of human blood plasma // *Optics and Spectroscopy*, **112**(6), p. 884-892 (2012).
43. Yu.A. Ushenko, Yu.Ya. Tomka, A.V. Dubolazov, Laser diagnostics of anisotropy in birefringent networks of biological tissues in different physiological conditions // *Quantum Electronics*, **41**(2), p. 170-175 (2011).
44. Yu.A. Ushenko, A.V. Dubolazov, V.O. Balanetskaya, A.O. Karachevtsev, V.A. Ushenko, Wavelet-analysis of polarization maps of human blood plasma // *Optics and Spectroscopy*, **113**(3), p. 332-343 (2012).